Formation of α-Mn and R structures from the β-Mn structure in Mn-Si alloys

T. Doi,[1] T. Kobayashi,[1] M. Tanimura,[2] and Y. Koyama[1]
[1]*Department of Electronic and Photonic Systems and Kagami Memorial Laboratory for Materials Science and Technology, Waseda University, Shinjuku, Tokyo 169-8555, Japan*
[2]*Research Department, NISSAN ARC Limited, Yokosuka, Kanagawa 237-0061, Japan*
(Received 23 July 2010; revised manuscript received 18 September 2010; published 19 November 2010)

The Mn-Si alloy system undergoes the (β-Mn$\rightarrow\alpha$-Mn+R) eutectoid reaction at 908 K around 8 at. % Si. The crystal structures of the β-Mn, α-Mn, and R phases were reported to consist of complex coordination polyhedra such as a polyhedron with coordination number (CN) 12: that is, an icosahedral atomic cluster. The notable features of these structures are that both the α-Mn and R structures are characterized by arrays of penetrated CN16 pairs while penetrated CN14 pairs are present in the β-Mn structure. In a penetrated CN16 pair consisting of two CN16 polyhedra, for instance, a center atom of one CN16 polyhedron is one of 16 atoms forming a shell of the other. To understand the crucial factors controlling a change between two coordination-polyhedra structures, in this study, the crystallographic features of the (β-Mn$\rightarrow\alpha$-Mn) and (β-Mn$\rightarrow R$) structural changes related to the eutectoid reaction have been investigated by transmission electron microscopy. It was found that the former (β-Mn$\rightarrow\alpha$-Mn) change started with the conversion of a penetrated CN14 pair into a penetrated CN16 pair by successive and simple atomic shifts. Among three types of orientation relations between the β-Mn and R structures in the latter change, the direct conversion of a penetrated CN16 pair from a penetrated CN14 pair should first occur for the major relation. As for two other minor relations found mainly for higher Si contents, in the starting changes, a penetrated pair consisting of CN14 and CN12 polyhedra, and two neighboring CN14 and CN12 polyhedra in the β-Mn structure must be converted to a penetrated CN16 pair, and two neighboring CN16 and CN12 polyhedra in the R structure, respectively. The directional relation in the orientation relationship for these two structural changes was, as a result, determined by orientations of the penetrated CN14 pairs or two neighboring polyhedra in the β-Mn structure. It is thus understood that the crucial factor controlling the (β-Mn$\rightarrow\alpha$-Mn) and (β-Mn$\rightarrow R$) structural changes should be the conversion between the structural units consisting of only two neighboring polyhedra, which are involved in these complex structures. Furthermore, both site occupancies of atoms and atomic-bond lengths in the penetrated CN16 pairs for the α-Mn and R structures were evaluated to understand the physical origin of interplay between the appearance of a magnetic moment in the former structure and the formation of covalentlike atomic bonding in the latter.

DOI: 10.1103/PhysRevB.82.184205 PACS number(s): 71.20.Lp, 71.20.Be, 68.37.Lp, 75.50.Ee

I. INTRODUCTION

In 1984, Shechtman *et al.*[1] reported the presence of the quasicrystal in rapidly quenched Al-Mn alloys. It is now recognized that the quasicrystal is characterized by the break of the translational and rotational symmetries that are allowed in the three-dimensional crystallography.[2–5] The finding of quasicrystals and related approximant phases also gives us the importance of crystal structures consisting of atomic clusters in alloys. One of basic structural units for atomic clusters in quasicrystals is obviously a coordination polyhedron with coordination number (CN) 12: that is, an icosahedral atomic cluster.[6–14] In addition to the CN12 polyhedra, the dodecagonal quasicrystal was suggested to consist of atomic columns that are basically formed by a one-dimensional connection of CN14 polyhedra.[15,16]

There exist CN12 polyhedra as a local structural unit in metallic glasses.[17–20] Recently, CN16 polyhedra were also found in an Fe-based bulk metallic glass with a high glass stability.[21–26] Based on these findings, the strong suppression for the crystallization in metallic glasses was discussed in terms of both the formation and the stability of these polyhedra. The interesting point to note here is that amorphous state in Fe-Nb-B alloys was reported to exhibit nanoscale structural and compositional changes related to the phase separation to the (bcc+α-Mn) state in an earlier stage of the crystallization. This suggests that CN16 polyhedra involved in the α-Mn structure may be present in the amorphous state of Fe-Nb-B alloys, just as in the case of the Fe-based bulk metallic glass.[27] Based on these results, an understanding of both the formation and the stability of coordination polyhedra, and the crystallographic relation between these polyhedra should be required for a deeper understanding of metallic-glass and amorphous states as well as quasicrystals in alloys. However, it is hard to examine their detailed features because of the extremely complex atomic arrangements in quasicrystals and the arrangements without long-range ordering in metallic-glass and amorphous states. In this study, thus, we focused on three coordination-polyhedra structures involving CN14 or CN16 polyhedra to understand both the formation of a CN16 polyhedron and the crystallographic relation between the CN14 and CN16 polyhedra. Concretely, we have investigated their detailed features by using the (β-Mn$\rightarrow\alpha$-Mn+R) eutectoid reaction in the Mn-Si alloy system.

Manganese is known to be one of the most complex metallic elements. When the temperature is lowered from the liquid state, the metallic Mn undergoes ($\delta\rightarrow\gamma\rightarrow\beta\rightarrow\alpha$) successive phase transitions in the solid state.[28–30] Among these

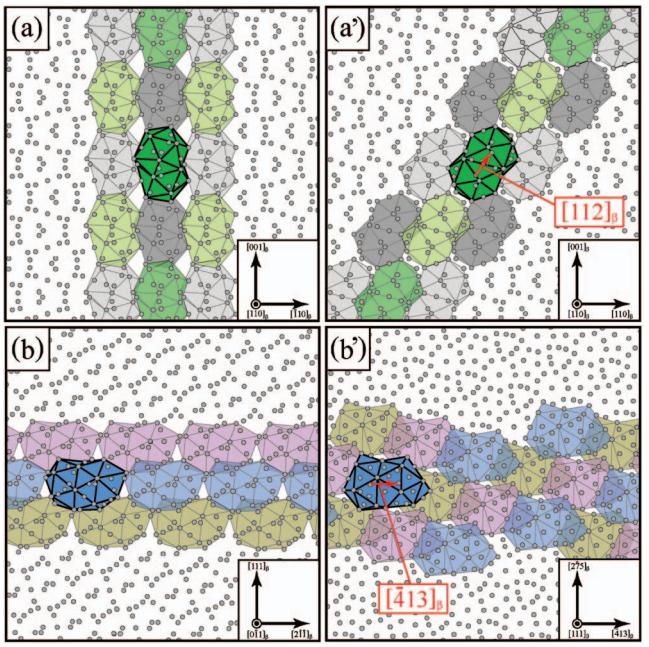

FIG. 1. (Color) Projections of the atomic positions in the β-Mn structure. The projected directions in (a), (a′), (b), and (b′) are, respectively, parallel to the $[110]_\beta$, $[1\bar{1}0]_\beta$, $[0\bar{1}1]_\beta$, and $[111]_\beta$ directions. The atomic positions reported by Shoemaker *et al.* (Ref. 34) were used for these diagrams. In the β-Mn structure, penetrated CN14 pairs with the $[112]_\beta$ connected direction are arranged periodically, as indicated by the colored regions in (a) and (a′), while the regular array of penetrated CN14 pairs with the $[\bar{4}13]_\beta$ connected direction can be detected, as drawn by the colored regions in (b) and (b′). In one penetrated CN14 pair consisting of two CN14 polyhedra, a center atom in one CN14 polyhedron is one of 14 atoms forming a shell of the other. The connected direction is also referred to as a direction connected between two center atoms in one penetrated CN14 pair. The difference in the colors for these regions is just a visual guide to easily understand the spatial correspondence among the penetrated CN14 pairs.

four phases, the δ and γ phases present in higher temperatures have the usual bcc and fcc structures, respectively. The β-Mn and α-Mn structures of the β and α phases in lower temperatures were, on the other hand, reported to be very complicated crystal structures involving coordination polyhedra such as a CN12 polyhedron.[31–34] In addition, the interesting feature in Mn-rich alloys is that in the Mn-Si alloy system, for instance, the R (Mn_6Si) phase, another coordination-polyhedra phase, appears around 13 at. % Si.[35,36] As a result of the appearance of the R phase, there is a (β-Mn$\rightarrow\alpha$-Mn+R) eutectoid reaction that is characterized by structural changes between coordination-polyhedra structures.[37] Although we have so far studied the formation of the coordination-polyhedra structures from the bcc structure in the Fe-Mo and Cr-Co alloy systems,[38–42] the presence of this eutectoid reaction presents us with the following question: "what are the crucial factors controlling a structural change between two coordination-polyhedra structures?" To understand such factors, we have examined the crystallographic features of the (β-Mn$\rightarrow\alpha$-Mn) and (β-Mn$\rightarrow R$) structural changes in the Mn-Si alloy system by transmission electron microscopy.

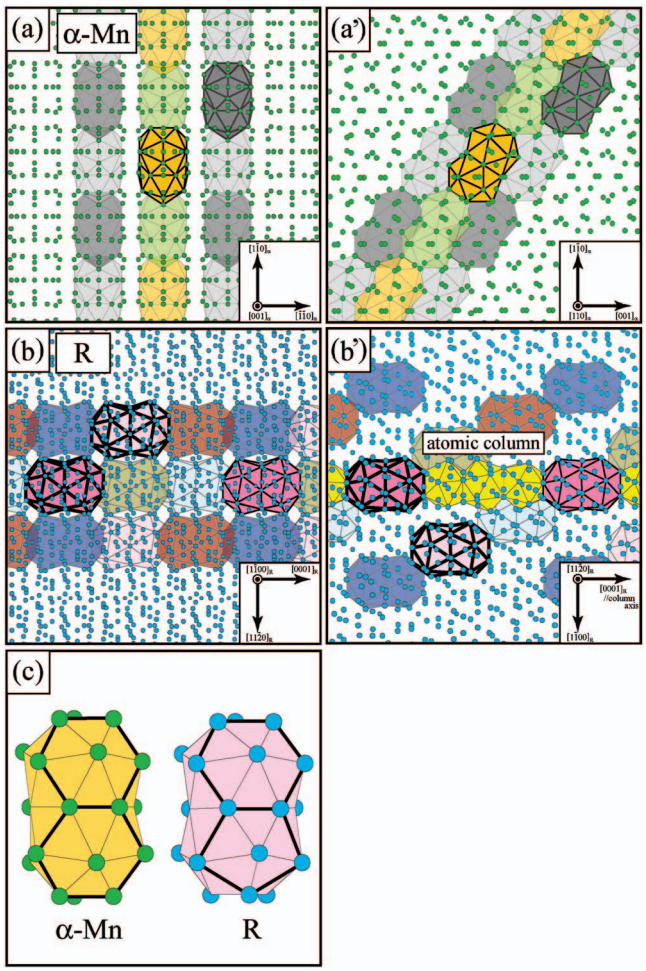

FIG. 2. (Color) Projections of the atomic positions in the α-Mn and R structures. The $[001]_\alpha$ and $[110]_\alpha$ projections of the α-Mn structure are, respectively, depicted in (a) and (a′) while the diagrams in (b) and (b′) show the $[1\bar{1}00]_R$ and $[11\bar{2}0]_R$ projections of the R structure. The penetrated CN16 pairs involved in the α-Mn and R structures are also shown in (c). The crystallographic data reported by Bardos *et al.* and Shoemaker *et al.* (Ref. 36) were, respectively, used for the atomic positions in the α-Mn and R structures (Ref. 33). Note that, in one penetrated CN16 pair, a center atom in one CN16 polyhedron is one of 16 atoms forming a shell of the other, just like a penetrated CN14 pair in the β-Mn structure. In the figure, the regular arrays of penetrated CN16 pairs in the α-Mn and R structures are indicated by the colored regions in (a) and (a′), and (b) and (b′), respectively. The difference in the colors for these regions is a visual guide to understand the spatial correspondence among the penetrated CN16 pairs. It is also understood that the difference between the penetrated CN16 pairs in the α-Mn and R structures is the connection between two CN16 polyhedra, as indicated by the thick lines in (c).

Figure 1 shows the $[110]_\beta$, $[1\bar{1}0]_\beta$, $[0\bar{1}1]_\beta$, and $[111]_\beta$ projections of the β-Mn structure as the initial structure in the (β-Mn$\rightarrow\alpha$-Mn or R) structural change. The β-Mn structure with the cubic symmetry involves 20 atoms in a unit cell, and there are two Mn sites, Mn I and Mn II, even for the crystal structure of the metallic Mn.[34] The feature of the structure as a coordination-polyhedra structure is that a CN

14 polyhedron is formed around each Mn II site while the polyhedron formed around the Mn I site can be identified as a distorted CN 12 one. The interesting feature of the β-Mn structure is that there is a pair consisting of two CN 14 polyhedra in which a center atom in one polyhedron is one of 14 atoms forming a shell of the other. In this study, this unique CN14 pair and the connected direction between the two center atoms in it are referred to as the penetrated CN14 pair and the connected direction, respectively. The point to note here is that penetrated CN14 pairs are periodically arranged in the β-Mn structure. In Fig. 1, penetrated CN14 pairs with the $[112]_\beta$ connected direction are shown as colored regions in (a) and (a′) while colored regions in (b) and (b′) correspond to penetrated CN14 pairs with the $[\bar{4}13]_\beta$ direction. Note that the difference in the colors for these regions is just a visual guide to easily understand the spatial distribution for these two types of penetrated CN14 pairs.

Both the $[001]_\alpha$ and $[110]_\alpha$ projections of the α-Mn structure with the cubic symmetry and the $[1\bar{1}00]_R$ and $[11\bar{2}0]_R$ projections of the R structure with the trigonal symmetry are schematically depicted in Fig. 2, together with the schematic diagram of the penetrated CN16 pairs in the α-Mn and R structures. Note that the crystallographic directions and planes in the R structure are indexed in terms of the hexagonal system, instead of the trigonal one. According to previous studies,[33,36] it has been reported that there are CN12, CN13, and CN16 polyhedra in the α-Mn structure consisting of 58 atoms in a unit cell, and CN12, CN14, CN15, and CN16 ones in the R structure of 159 atoms. In spite of the presence of various coordination polyhedra, the notable feature of the α-Mn and R structures is that these structures commonly involve penetrated pairs consisting of two CN16 polyhedra. The array of penetrated CN16 pairs in the α-Mn structure is indicated by the colored regions in (a) and (a′) while the colored regions in (b) and (b′) correspond to penetrated CN16 pairs in the R structure. The difference in the colors is also a visual guide to understand the spatial distribution for the penetrated CN16 pairs, just as in Fig. 1 for the β-Mn structure. The point to note here is that there is a difference between the penetrated CN16 pairs in the α-Mn and R structures with respect to the connection between the two CN16 polyhedra forming a penetrated pair, as indicated by the thick lines in (c). From the similarity between the arrays of the penetrated CN14 and CN16 pairs shown in Figs. 1 and 2, it is likely that the penetrated CN16 pairs in the α-Mn structure and R structures may have some relation to the penetrated CN14 pair in the β-Mn structure, and would play a certain role in both the (β-Mn$\rightarrow\alpha$-Mn) and (β-Mn$\rightarrow R$) structural changes related to the eutectoid reaction.

In the Fe-Mo alloy system, the R structure appears as the crystal structure of the Fe_3Mo_2 phase in the temperature range between 1473 and 1761 K.[43] We have previously examined the crystallographic features of the formation of the R structure from the bcc structure by using the (bcc$\rightarrow$bcc $+R$) reaction in this alloy system.[42] The experimental data obtained by transmission electron microscopy revealed that the R structure was characterized by a periodic array of atomic columns consisting of both CN12 polyhedra and penetrated CN16 pairs. Note that the one-dimensional alternating array of pink and yellow regions along the $[0001]_R$ direction in Fig. 2(b′) corresponds to an atomic column as one of the structural units in the R structure. Note that the yellow region consists of three neighboring CN12 polyhedra. According to our previous study, shorter atomic bonds reflecting a covalentlike character are present between Fe atoms forming a shell of a penetrated CN16 pair as another structural unit. Instead of the formation of covalentlike bonding in the R structure, on the other hand, complicated antiferromagnetic ordering has been reported in the α-Mn structure.[33,44–49] Based on these observations, we are very interested in the interplay between the appearance of a magnetic moment and the formation of covalentlike bonding in crystal structures involving larger CN polyhedra such as a CN16 polyhedron. Thus, in this study we focus on the formation of penetrated CN16 pairs from the β-Mn structure involving penetrated CN14 pairs. To understand the critical factors controlling a structural change between two coordination-polyhedra structures, we have investigated the crystallographic features of both the (β-Mn$\rightarrow\alpha$-Mn) and (β-Mn$\rightarrow R$) structural changes in Mn-Si alloys by transmission electron microscopy. Below we will describe the detailed results concerning these two structural changes, which were obtained in this study.

II. EXPERIMENTAL PROCEDURE

The (β-Mn$\rightarrow\alpha$-Mn$+R$) eutectoid reaction was reported as occurring at 908 K around 8 at. % Si in the Mn-Si alloy system.[37] In this study, the crystallographic features of the (β-Mn$\rightarrow\alpha$-Mn) and (β-Mn$\rightarrow R$) structural changes related to the reaction were, respectively, examined mainly by using Mn-(7, 8, 9, 10, and 11) at. % Si alloy samples. Ingots of these alloys were prepared from Mn and Si with purity of 99.9% by an induction melting technique. The ingots were kept at 1273 K in the single β-Mn region for 24 h to get the metastable β-Mn state, followed by quenching in ice water. To induce the (β-Mn$\rightarrow\alpha$-Mn) structural change, metastable β-Mn alloy samples with composition of (7 and 8) at. % Si, cut from the ingots, were annealed at 873 K in vacuum for various annealing times. The annealing temperature of 873 K was also used for the (β-Mn$\rightarrow R$) change in Mn-(8, 9, 10, and 11) at. % Si samples. The crystallographic features of these annealed samples were examined at room temperature, using JEM-3010- and 1010-type transmission electron microscopes with accelerating voltages of 300 kV and 100 kV, respectively. Specimens for our observation made by transmission electron microscopy were prepared by an Ar-ion thinning technique.

III. EXPERIMENTAL RESULTS

A. Crystallographic features of the (β-Mn$\rightarrow\alpha$-Mn) structural change

Of the structural changes related to the (β-Mn$\rightarrow\alpha$-Mn $+R$) reaction, we first describe the experimental results on the crystallographic features of the (β-Mn$\rightarrow\alpha$-Mn) change. The experimental data concerning this change were collected from Mn-(7 and 8) at. % Si alloy samples with a meta-

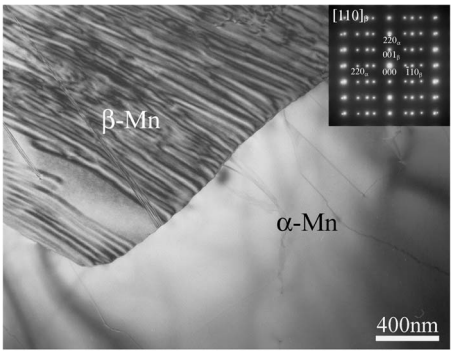

FIG. 3. Bright field image of the (α-Mn+β-Mn) coexisting state in a Mn-7 at. % Si alloy sample annealed for 3 h together with the corresponding electron diffraction pattern. The electron beam incidence for both the image and the pattern is parallel to the $[110]_\beta$ direction. The complex contrast is seen in the upper-left β-Mn region. The pattern clearly indicates the presence of the unique orientation relationship between the α-Mn and β-Mn structures.

stable β-Mn state as an initial state and were annealed at 873 K for various annealing times. Figure 3 shows a bright field image of the (α-Mn+β-Mn) coexisting state in a Mn-7 at. % Si alloy sample annealed for 3 h. The electron beam incidence of the image is parallel to the $[110]_\beta$ direction. In the image, there are two areas divided by a boundary and a complex contrast is detected in the upper left area. The analysis of the corresponding electron diffraction patterns in the inset confirmed that the crystal structures in the upper-left and other areas were identified as the β-Mn and α-Mn structures, respectively. This implies that the complex contrast found in the β-Mn region is annihilated in the α-Mn region, which should be produced by the (β-Mn$\rightarrow\alpha$-Mn) structural change. Based on this, it is likely that the contrast is due to a structural defect that is associated with the appearance of the α-Mn structure.

To determine the orientation relationship between the α-Mn and β-Mn structures, we took electron diffraction patterns of the (α-Mn+β-Mn) coexisting state. We found that there was only one simple orientation relation between these two structures. Three electron diffraction patterns indicating this relation are shown in Fig. 4. The electron beam incidences in (a), (b), and (c) are, respectively, parallel to the $[110]_\beta$, $[1\bar{1}0]_\beta$, and $[11\bar{2}]_\beta$ directions. The surprising feature to note here is that, as seen in (b), the $[1\bar{1}0]_\beta$ pattern seems to come from a single crystal structure. Because the extinction rule of reflections for the β-Mn structure is obviously different from that for the α-Mn one, reflections due to the former structure must overlap those due to the latter. Taking this into account, we have the very simple relation of $(110)_\beta \| (002)_\alpha$ and $[1\bar{1}0]_\beta \| [110]_\alpha$. In addition, the lattice parameters of the α-Mn and β-Mn structures, a_α and a_β, with the cubic system are basically satisfied with the relation of $a_\alpha = \sqrt{2}a_\beta$. It was, in fact, confirmed that the value of a_α/a_β was estimated to be $a_\alpha/a_\beta \fallingdotseq 1.41$ by using the experimentally obtained lattice parameters of $a_\alpha = 8.84$ nm and $a_\beta = 6.25$ nm.

In Fig. 3, the complex contrast is observed in the β-Mn area in the (α-Mn+β-Mn) coexisting state. The contrast is

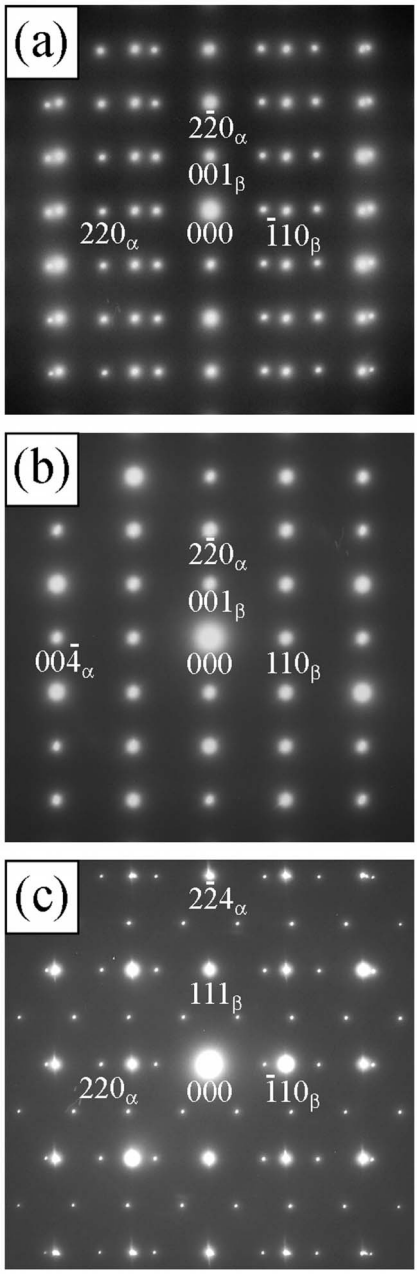

FIG. 4. Three electron-diffraction patterns indicating the single orientation relationship between the α-Mn and β-Mn structures. These patterns were taken from the (α-Mn+β-Mn) coexisting state in a Mn-7 at. % Si alloy sample annealed for 3 h. The electron beam incidences in (a), (b), and (c) are, respectively, parallel to $[110]_\beta$, $[1\bar{1}0]_\beta$, and $[11\bar{2}]_\beta$ directions. Based on the analysis of the patterns, the orientation relation was determined to be $(110)_\beta \| (002)_\alpha$ and $[1\bar{1}0]_\beta \| [110]_\alpha$. As a result of the simple relation, the pattern with the $[1\bar{1}0]_\beta$ incidence in (b) seems to come from a single state.

due to structural defects that should be associated with the (β-Mn$\rightarrow\alpha$-Mn) structural change. To understand the features of the initial change in the structural change, then, we examined the crystallographic features of β-Mn areas in Mn-7 at. % Si alloy samples with shorter annealing times. Figure 5 shows bright and dark field images of a β-Mn area

in a sample annealed for 30 min, together with a corresponding $[1\bar{1}0]_\beta$ electron diffraction pattern. We first looked at the pattern in (b). In that pattern, there are reflections due to the crystal structure of this area and strong streaks are seen along the $[11\bar{1}]_\beta$ line around each reflection. Although the analysis of diffraction patterns with other electron beam incidences indicated that the area had the β-Mn structure, the $[1\bar{1}0]_\beta$ pattern in (b) looks like the $[110]_\alpha$ pattern of the α-Mn structure. Based on this, it seems to us that a certain structural change to the α-Mn structure should already have occurred in the β-Mn area. In the bright field image, in fact, we see thin regions along the $[112]_\beta$ direction. Both the violation of the extinction rule for the β-Mn reflections and the presence of the streaks in the pattern suggest that the thin region can be identified as a transitional state related to the formation of the α-Mn structure. To confirm this, the dark field image in (c) was taken by using the forbidden 003_β reflection for the β-Mn structure. The thin regions are actually observed as bright contrast in the dark β-Mn matrix. Because the forbidden 003_β reflection is allowed for the α-Mn structure, a transitional state as the starting state should appear in such thin regions. It is thus understood that the (β-Mn$\rightarrow\alpha$-Mn) structural change presumably occurs by successive structural changes, not a direct one.

To understand the detailed features of the transitional state, we took high-resolution electron micrographs of thin regions appearing in the shorter annealing times. Figure 6 shows a bright field image, a high-resolution electron micrograph, and a calculated micrograph of a β-Mn matrix involving the transitional state in a 30-min-annealed sample. The corresponding $[1\bar{1}0]_\beta$ electron diffraction pattern is also shown in the inset. A thin region as a transitional state is clearly seen in the image, and there are both forbidden reflections for the β-Mn structure and a streak around each reflection in the pattern. The interesting feature of the image is that a boundary between the β-Mn matrix and the transitional-state region is rather diffuse. In addition, the region surrounded by the red lines in the image exhibits a complicated contrast in the experimental micrograph, (b). It is hard to interpret the detailed features of the contrast in the transitional-state region by using the experimental micrograph. To clarify the features of the region, we reproduced the calculated micrograph in (c) from the experimental one in (b) by using the reflections indicated by the arrows in the pattern. Interestingly, the characteristic contrast is reproduced in the calculated micrograph, where the transitional-state region is located at the middle. To understand the features of the contrast in the β-Mn matrix, first, the contrast in the calculated micrograph is compared with the $[1\bar{1}0]_\beta$ projection of the β-Mn structure shown in (c). The comparison clearly indicates that projected positions of atoms are densely arranged in the dark-contrast regions of the calculated micrograph. In other words, the understanding of this is that the contrast in the calculated micrograph basically reflects the projected positions of atoms in the β-Mn structure. The green region in (c) actually corresponds to a penetrated CN14 pair. Keeping this correspondence in mind, we focus on the contrast in the transitional-state region at the middle. Although it is hard to find conspicuous contrast that is different from the contrast in the β-Mn matrix, a bright-contrast ring with a radius of about 0.3 nm can be detected in the interior of the thin white square indicated in the calculated micrograph. The important feature of the bright-contrast ring

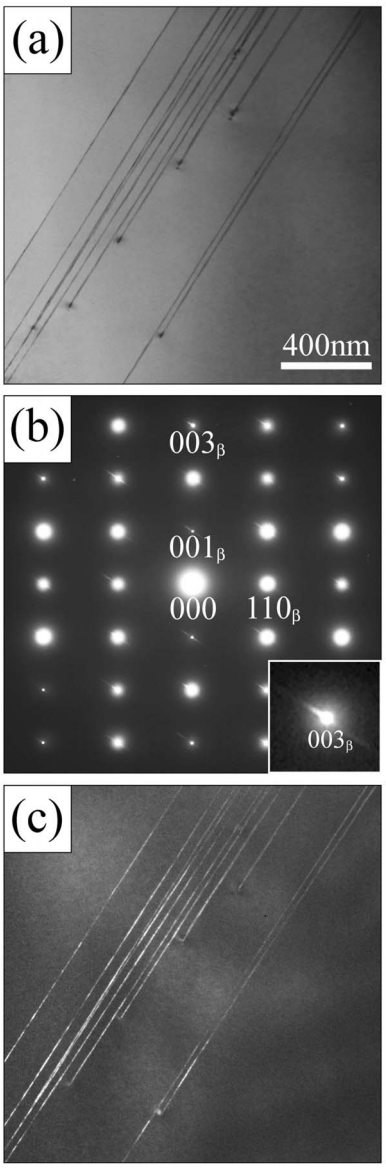

FIG. 5. Bright and dark field images obtained from a β-Mn matrix involving the transitional state together with a corresponding electron diffraction pattern with the $[1\bar{1}0]_\beta$ electron incidence. The enlarged pattern in the vicinity of the 003_β reflection is also shown in the inset. The images and the pattern were taken from a Mn-7 at. % Si alloy sample annealed for 30 min. In the bright field image, (a), dark-contrast lines are seen in a β-Mn matrix. In addition, there exist both forbidden reflections for the β-Mn structure such as the 003_β reflection and a streak through each reflection along the $[11\bar{1}]_\beta$ direction in pattern, (b). Note that the streak can easily be detected in the inset. Furthermore, the dark-contrast lines in (a) are observed as bright contrast in the dark field image, (c), which was taken by using the 003_β forbidden reflection. This implies that the dark-contrast line in (a) should originate from the transitional state in the (β-Mn$\rightarrow\alpha$-Mn) structural change.

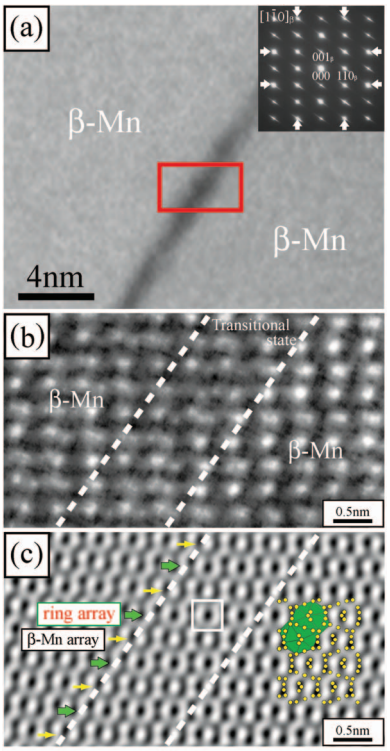

FIG. 6. (Color) Bright field image, a high-resolution electron micrograph, and a calculated micrograph of a β-Mn matrix involving the transitional state, together with a corresponding $[1\bar{1}0]_\beta$ electron-diffraction pattern in the inset of (a). The image, micrographs, and pattern were taken from the Mn-7 at. % Si alloy sample annealed for 30 min, which is the same as that used in Fig. 5. In the image, (a), a line-shaped transitional state was observed as dark contrast in a β-Mn matrix and the boundary between the state and the β-Mn matrix is obscure. To understand the detailed features of the transitional state, the experimental micrograph in (b) was taken from the area indicated by the red square in (a). The defocus value and the sample thickness for the experimental micrograph were, respectively, estimated to be about -80 nm and about 10 nm. The micrograph in (b) exhibits the complex contrast and we then reproduced the calculated micrograph in (c) from the experimental one in (b) by using the reflections indicated by the arrows in the pattern. In (c), the small yellow circles and the green region in the β-Mn area indicate projected positions of atoms along the $[1\bar{1}0]_\beta$ direction and a penetrated CN14 pair with the $[112]_\beta$ connected direction in the β-Mn structure, respectively. The interesting feature is that bright-contrast rings are seen in the interior of the transitional state, as indicated by the white square. As a result of the appearance of the bright-contrast ring, the transition state is characterized by the alternating arrangement of the ring and β-Mn arrays, as marked by the thick green and thin yellow arrows, along the vertical direction in (c). In the calculated micrograph, the dark-contrast region in the β-Mn area basically corresponds to the region in which projected positions of atoms are densely arranged.

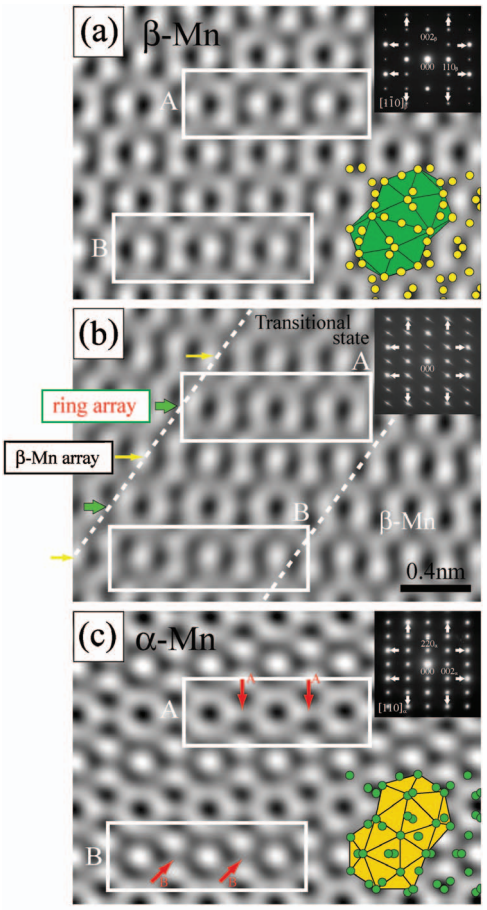

FIG. 7. (Color) Calculated micrographs of the β-Mn, transitional-state, and α-Mn regions, together with their corresponding electron diffraction patterns in the insets. The electron beam incidences are parallel to the $[1\bar{1}0]_\beta$ direction for (a) and (b), and the $[110]_\alpha$ direction for (c). These calculated micrographs were reproduced from high-resolution electron micrographs obtained experimentally by using the reflections indicated by the arrows in the corresponding patterns. The experimental micrographs for the β-Mn and transitional-state regions were taken from the 30-min-annealed Mn-7 at. % Si alloy sample, under the same condition of the defocus value and the sample thickness as that in Fig. 6. On the other hand, a Mn-7 at. % Si sample annealed for 150 h was used for taking the experimental micrograph of the α-Mn structure with the defocus value of about -80 nm and the sample thickness of about 10 nm. In (a), further, the projected positions of the atoms and a penetrated CN14 pair in the β-Mn structure are, respectively, indicated by the small yellow circles and the green region, while the small green circles and the orange region in (c) represent the projected positions of atoms and a penetrated CN16 pair in the α-Mn structure. From these micrographs, we can see the characteristic contrast changes in the ring and β-Mn arrays, which reflect the (β-Mn$\rightarrow\alpha$-Mn) structural change, as indicated by the white rectangles A and B.

is that the rings are arranged along the horizontal $[110]_\beta$ direction in the thin region, as indicated by the green thick arrows. Based on this, the array of bright-contrast rings is here referred to as a ring array. As a result of the appearance of the ring array in the thin-banded region, the remaining contrast for the β-Mn structure forms the β-Mn array, as indicated by the yellow thin arrows. The understanding of this is that the contrast in the transitional-state region is characterized by the alternating arrangement of the ring and β-Mn arrays along the perpendicular $[001]_\beta$ direction, as marked by the thick green and thin yellow arrows.

The contrasts of both the β-Mn matrix and the transitional-state region in the calculated $[1\bar{1}0]_\beta$ micrograph are compared with the contrast of the α-Mn precipitate. High-resolution electron micrographs of the α-Mn precipitate were taken from the Mn-7 at. % Si sample annealed for 150 h. Calculated micrographs of the β-Mn matrix, the transitional-state region, and the α-Mn precipitate are shown in Fig. 7, together with both their corresponding electron-diffraction patterns and the projections of the β-Mn and α-Mn structures. The calculated micrograph in (c) was reproduced from an experimental micrograph by using the reflections indicated by the small arrows in the pattern. Based on the comparison between the contrast in the calculated micrograph and the projected positions of the atoms in the α-Mn structure, first, it is found that dark-contrast regions in the micrograph basically correspond to regions, in which projected positions of atoms are densely arranged. We then focus on the contrast change shown in these calculated micrographs. It is confirmed that the first change from the β-Mn structure to the transitional state is the formation of a ring array along the $[110]_\beta$ direction, as seen in the regions surrounded by White rectangle A in (b). The second change from the transitional state to the α-Mn structure involves the following three steps. One step is the appearance of the bright-contrast line connected between two neighboring bright rings in the ring array, as indicated by Arrows A in White rectangle A of (c). The others are the formations of both a dark-contrast ring and a dark-contrast line between two neighboring dark rings in the β-Mn array. The dark-contrast rings are clearly seen in the interior of white rectangle B in (c) and the dark-contrast lines are indicated by arrows B in it. The presence of these changes and steps, suggests that the (β-Mn$\rightarrow\alpha$-Mn) structural change via the transitional state should take place by successive and simple atomic shifts. Based on these calculated micrographs, we conclude that these atomic shifts are associated with the formation of a penetrated CN16 pair from a penetrated CN14 one. In other words, the transitional configuration between the penetrated CN14 and CN16 pairs may be present in the (β-Mn$\rightarrow\alpha$-Mn) structural change. Note that the green region in (a) and the orange region in (c) indicate the penetrated CN14 pair in the β-Mn structure and the penetrated CN16 pair in the α-Mn CN16 pair, respectively.

B. Crystallographic features of the (β-Mn$\rightarrow R$) structural change

In this study, the experimental data concerning the (β-Mn$\rightarrow R$) structural change were collected by using Mn-(8, 9, 10, and 11) at. % Si alloy samples. As in the case of the (β-Mn$\rightarrow\alpha$-Mn) change, we started with the examination of the orientation relationship between the β-Mn and R structures. We determined that the crystallographic direction of the β-Mn structure is parallel to the $[0001]_R$ direction in the R structure. It is obvious that the atomic column in the R structure has the column axis along the $[0001]_R$ direction. We found that there were three types of orientation relations between the β-Mn and R structures, which are here denoted by $R1$, $R2$, and $R3$. The $[0001]_R$ column axes for the $R1$, and $R2$, and $R3$ relations are, respectively, nearly parallel to the $\langle 134\rangle_\beta$, $\langle 120\rangle_\beta$, and $\langle 130\rangle_\beta$ directions in the β-Mn structure. The points to note here are that the $R2$ and $R3$ relations were mainly found in alloys with higher Si contents, and that the frequencies for finding these three relations were estimated to be $R1:R2:R3=70:15:15$. Based on this ratio, the $R1$ relation can be regarded as the major relation while the others are referred to as the minor ones.

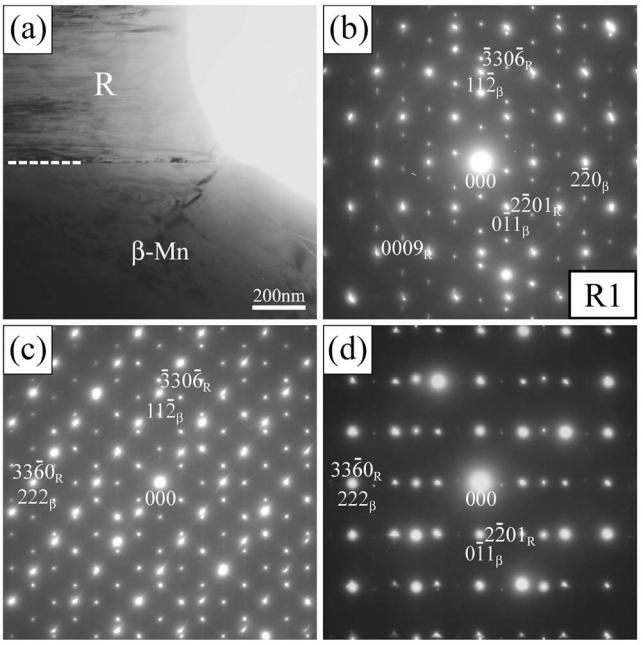

FIG. 8. Bright field image and three corresponding electron-diffraction patterns of the (β-Mn+R) coexisting state in a Mn-11 at. % Si alloy sample annealed at 873 K for 3 h. The electron beam incidences in (a) and (b), (c), and (d) are, respectively, parallel to the $[111]_\beta$, $[1\bar{1}0]_\beta$, and $[2\bar{1}\bar{1}]_\beta$ directions. In (a), R and β-Mn regions separated by a straight boundary, as indicated by the white dashed lines, are present in the upper and lower areas in the image. The patterns indicate the presence of the major $R1$ relation, $(0\bar{1}1)_\beta \| (2\bar{2}01)_R$ and $[111]_\beta \| [11\bar{2}0]_R$, between the β-Mn and R structures.

We first describe the experimental data on the major $R1$ relation. Figure 8 shows three electron diffraction patterns of the (β-Mn+R) coexisting state for the major relation together with a corresponding bright field image. Both the image and the pattern were taken from a Mn-11 at. % Si alloy sample annealed at 873 K for 3 h. The electron beam incidences of the patterns in (b), (c), and (d) are, respectively, parallel to the $[111]_\beta$, $[1\bar{1}0]_\beta$, and $[2\bar{1}\bar{1}]_\beta$ directions, and the image was taken in the $[111]_\beta$ incidence. In the image, we clearly see two areas separated by a sharp boundary. The feature of the image is that a complex contrast is observed only in the upper area while the lower area exhibits relatively uniform contrast. Based on the analysis of the patterns, it was confirmed that the lower and upper areas had the β-Mn and R structures, respectively. This implies that structural defects giving rise to the complex contrast are involved only in the R-structure area. The situation concerning structural

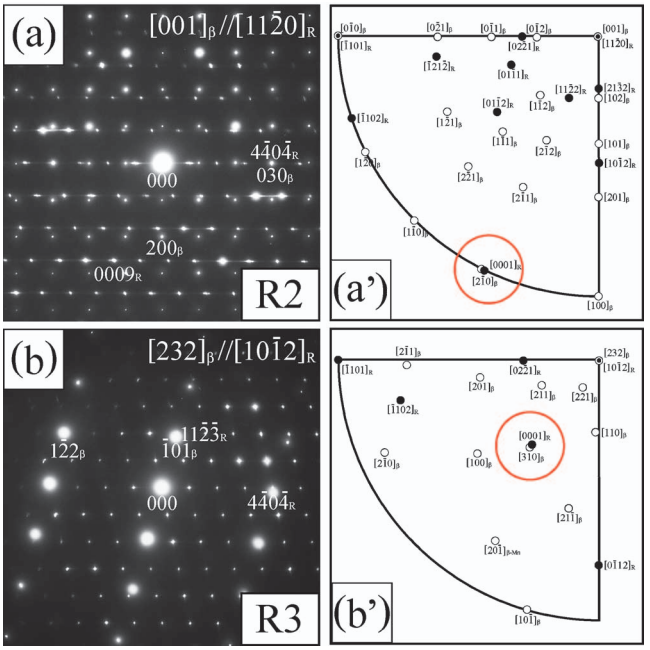

FIG. 9. (Color) Electron-diffraction patterns and corresponding pole figures indicating the minor $R2$ and $R3$ relations between the β-Mn and R structures. The patterns were taken from two different (β-Mn+R) coexisting areas in the same 3-h-annealed Mn-11 at. % Si alloy sample, and the electron beam incidences in (a) and (b) are, respectively, parallel to the $[001]_\beta$ and $[232]_\beta$ directions. Based on the constructed pole figures, it is found that the atomic column in the R structure has the $[0001]_R$ column axis that is parallel to the $[2\bar{1}0]_\beta$ direction for the $R2$ relation and to the $[310]_\beta$ direction for the $R3$ relation, as indicated by the red circles.

defects is obviously different from that in the (β-Mn $\rightarrow \alpha$-Mn) change. It is thus likely that there is a certain difference between the formation processes of penetrated CN16 pairs in the (β-Mn$\rightarrow\alpha$-Mn) and (β-Mn$\rightarrow R$) structural changes. As for the orientation relationship, we found that the major $R1$ relation is $(0\bar{1}1)_\beta \| (2\bar{2}01)_R$ and $[111]_\beta \| [11\bar{2}0]_R$, and that the $[0001]_R$ column axis of the atomic column in the R structure is nearly parallel to the $[\bar{4}13]_\beta$ direction in the β-Mn structure. Based on this, we can say that the direction of a column axis is not parallel to one of the low-index crystallographic directions in the β-Mn structure. This would be an indication that the formation of the atomic column is not an essential feature of the (β-Mn $\rightarrow R$) structural change. In other words, there is a possibility that the formation of a smaller structural unit in the R structure such as a penetrated CN16 pair may play an essential role in the structural change for the major $R1$ relation.

Figure 9 shows electron diffraction patterns indicating the minor $R2$ and $R3$ relations together with their corresponding pole figures. The patterns were taken from (β-Mn+R) coexisting regions in a Mn-11 at. % Si alloy sample annealed for 3 h. By using both the patterns and figures, we determined the following orientation relations: that is, $(030)_\beta \| (4\bar{4}0\bar{4})_R$ and $[001]_\beta \| [11\bar{2}0]_R$ for $R2$ and $(\bar{1}01)_\beta \| (11\bar{2}\bar{3})_R$ and $[232]_\beta \| [10\bar{1}2]_R$ for $R3$. The corresponding $[0001]_R$ column axis for the $R2$ and $R3$ relations are, respectively, found to be nearly parallel to the $[2\bar{1}0]_\beta$ and $[310]_\beta$ directions, as indicated by the red circles in the pole figures. It is thus understood that the column axes for the $R2$ and $R3$ relations are nearly parallel to the low-index directions in the β-Mn struc-

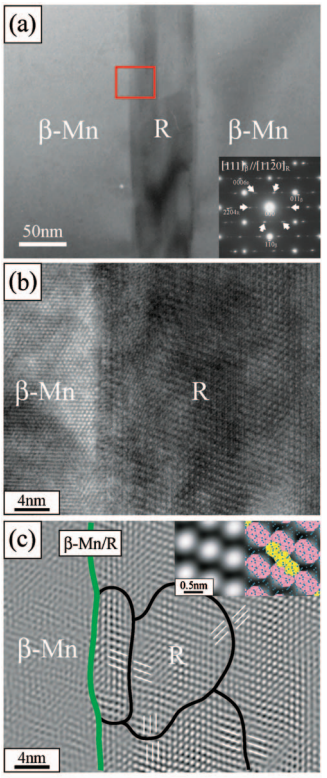

FIG. 10. (Color) Bright field image, high-resolution electron micrograph, and calculated micrograph of the (β-Mn+R) coexisting state with the $R1$ relation, together with a corresponding $[111]_\beta$ electron-diffraction pattern in the inset of (a). The image, pattern, and experimental micrograph were taken from a Mn-11 at. % Si alloy sample annealed at 873 K for 1 h. An R precipitate at the center of the image is seen as a dark-contrast region in a bright β-Mn matrix. In the experimental micrograph, (b), taken from the area indicated by the red square in (a), the R precipitate exhibits the relatively complex contrast. To understand the crystallographic features of the R precipitate, the calculated micrograph in (c) was reproduced from the experimental micrograph in (b) by using the reflections indicated by the arrows in the pattern. Both the enlarged micrograph and the projected positions of atoms in the R structure are also shown in the inset of (c). The comparison between the array of bright dots and the projected positions of atoms in the inset indicates that each bright dot corresponds to one penetrated CN16 pair marked by the pink region, not CN12 polyhedra by the yellow region. Note that the atomic column in the R structure is characterized by a one-dimensional alternating arrangement of pink and yellow regions. From the calculated micrograph in (c), it is then understood that the R precipitate consists of nanometer-sized regions. The black and green lines in (c) indicate out-of-phase boundaries between two neighboring nanometer-sized regions and a structural boundary between the R precipitate and the β-Mn matrix, respectively. As indicated by the thin white lines, further, there is a certain phase shift across an out-of-phase boundary with respect to an array of penetrated CN16 pairs.

ture, unlike the case of the major $R1$ relation.

In the (β-Mn$\rightarrow R$) structural change for the $R1$ relation, as mentioned above, there are structural defects in the R precipitate, instead of a β-Mn matrix in the (β-Mn $\rightarrow \alpha$-Mn) change. It should be noted that the presence of defects was confirmed to be one of the common features for the $R1$, $R2$, and $R3$ relations. To understand the detailed features of structural defects, we took high-resolution electron micrographs of alloy samples with shorter annealing times, mainly for the $R1$ relation. Figure 10 shows a bright field image, a high-resolution electron micrograph, and a calculated micrograph of a Mn-11 at. % Si alloy sample annealed for 1 h, together with the corresponding $[111]_\beta$ electron-diffraction pattern. In the image, we see a banded-shape R precipitate at the middle, which is sandwiched by a β-Mn matrix. It is confirmed that the orientation relation between the R precipitate and the β-Mn matrix satisfy the $R1$ relation. The micrograph in (b) was then taken from the (β-Mn+R) coexisting area involving a boundary, which is surrounded by the red lines in the image. In (b), we see a dotted contrast in the interior of the precipitate while a triangular array of bright dots is present in the β-Mn matrix. It is obvious that the triangular array of dots in the β-Mn matrix is due to the $[111]_\beta$ electron beam incidence. In spite of the characteristic dotted contrast in the R precipitate, unfortunately, it is hard to understand the crystallographic features of the R precipitate. To get enough information on the atomic arrangement in the precipitate, we reproduced the calculated micrograph in (c) from the experimental micrograph in (b) by using the reflections indicated by the arrows in the pattern. A local regular array of bright dots is clearly seen in the calculated micrograph. In other words, the precipitate is found to consist of nanometer-sized regions, each of which contains regularly arranged bright dots. Note that the curved black lines in (c) correspond to boundaries between two neighboring nanometer-sized regions. To understand what corresponds to each bright dot, further, the contrast in the calculated micrograph was compared with the $[11\bar{2}0]_R$ projection of the R structure in the inset, where the enlarged calculated micrograph is shown. It is understood that each dot corresponds to a penetrated CN16 pair indicated by the pink region. This implies that atomic columns characterized by the one-dimensional alternating arrangement of penetrated CN16 pairs (the pink regions) and CN12 polyhedra (the yellow region) in the R structure are formed locally in the precipitate. It is worth noting that the nanometer-sized column-cluster state already has been found in the (bcc $\rightarrow R$) structural change of the Fe-Mo alloy system.[42] The local and regular array of penetrated CN16 pairs is thus an indication that the nanometer-sized column-clusters state is also present in the (β-Mn$\rightarrow R$) change in the Mn-Si alloy system. It seems to us that the column-cluster state is one of the common features in the formation of the R structure. Based on the presence of the column-cluster state, we think that the complex contrast in the bright field image should be ascribed to out-of-phase boundaries with respect to an array of penetrated CN16 pairs.

In the (bcc$\rightarrow R$) structural change in the Fe-Mo alloy system, the development from the column-cluster state to the

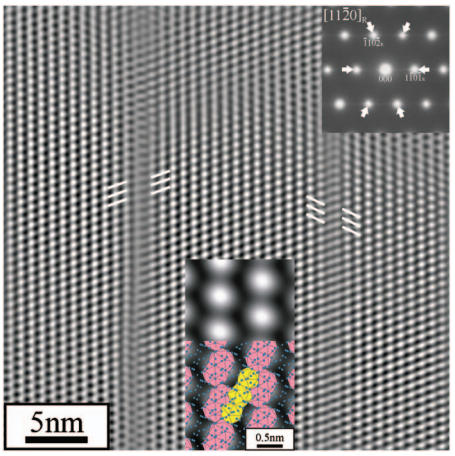

FIG. 11. (Color) Calculated micrograph of a R-structure region in the (α-Mn+R) coexisting state of a Mn-11 at. % Si alloy sample annealed at 873 K for 150 h together with a corresponding $[11\bar{2}0]_R$ electron-diffraction pattern in the inset. The micrograph was reproduced from an experimental micrograph by using the reflections indicated by the arrows in the pattern. Both the enlarged micrograph and the projected positions of atoms in the R structure are also shown in another inset, where the pink and yellow regions represent penetrated CN16 pairs and CN12 polyhedra, respectively. Each bright dot in the micrograph corresponds to one penetrated CN16 pair. In the R-structure region, nanometer-sized regions are well developed, but there still exist out-of-phase boundaries, as indicated by the parallel white lines.

R-structure state took place by the annihilation of out-of-phase boundaries separating nanometer-sized column-cluster regions.[42] To confirm this in the (β-Mn$\rightarrow R$) change, high-resolution electron micrographs of the R-structure area in the (α-Mn+R) equilibrium state were taken using a Mn-11 at. % Si alloy sample annealed for 150 h. Figure 11 shows a calculated micrograph reproduced from an experimental micrograph of an R-structure region in the (α-Mn +R) coexisting state, together with the corresponding $[11\bar{2}0]_R$ electron-diffraction pattern in the inset. Both the enlarged calculated micrograph and the $[11\bar{2}0]_R$ projection of the R structure are also shown in another inset and the reflections indicated by the arrows in the pattern were used for reproducing the calculated micrograph. A regular array of penetrated CN16 pairs observed as bright dots is clearly seen in a wide area of the micrograph. That is, the R-structure state is well developed in the sample. The interesting feature of the micrograph is that there still exist out-of-phase boundaries as a structural defect in the R structure. In the micrograph, it is easy to detect a phase shift occurring across the boundary, as marked by the white lines.

IV. DISCUSSION

The crystallographic features of the (β-Mn$\rightarrow \alpha$-Mn) and (β-Mn$\rightarrow R$) structural changes, as changes between coordination-polyhedra structures, were investigated by utilizing the (β-Mn$\rightarrow \alpha$-Mn+R) eutectoid reaction in the Mn-Si alloy system. The experimental data obtained in this

study revealed that the former (β-Mn$\rightarrow\alpha$-Mn) change started with the conversion of the penetrated CN14 pair into the penetrated CN16 pair by successive local and simple atomic shifts. In the case of the latter (β-Mn$\rightarrow R$) change, on the other hand, a nanometer-sized column-cluster state appears in the initial stage. In the later stage, the R-structure state develops from the column-cluster state by the annihilation of out-of-phase boundaries separating nanometer-sized column-cluster regions. The point to note here is that the column-cluster state can be characterized by a local and regular array of penetrated CN16 pairs involved in the atomic column of the R structure. This implies that, in the (β-Mn$\rightarrow R$) change, the direct conversion between the penetrated CN14 and CN16 pairs should occur in the starting change, unlike the successive conversion in the (β-Mn$\rightarrow\alpha$-Mn) change. Although there is a difference between the formation processes for the α-Mn and R structures, our experimental data clearly indicates that the formation of the penetrated CN 16 pairs should be a key factor in these two structural changes. Based on these experimental data, then, we discuss here both the crystallographic relations between the β-Mn and α-Mn structures, and between the β-Mn and R structures for the major $R1$ relation; that is, (1) an orientation relation between penetrated CN 14 pairs in the β-Mn structure and penetrated CN16 pairs in the α-Mn and R structures, (2) atomic shifts in the conversion between the penetrated CN14 and CN16 pairs as a starting change for the (β-Mn$\rightarrow\alpha$-Mn) and (β-Mn$\rightarrow R$) structural changes, and (3) the features of the formation process of the penetrated CN16 pair in the (β-Mn$\rightarrow\alpha$-Mn) change. As for the minor $R2$ and $R3$ relations for higher Si contents, we tried to look for structural units in the β-Mn and R structures that were converted to each other in the (β-Mn$\rightarrow R$) structural change. Furthermore, interplay between the appearance of a local magnetic moment in the α-Mn structure and the formation of covalent-like bonding in the R structure is also discussed by evaluating site occupancies of atoms and atomic-bond lengths of the penetrated CN16 pairs in the α-Mn and R structures.

We start with a discussion of the orientation relation between penetrated CN14 pairs in the β-Mn structure and penetrated CN16 pairs in the α-Mn and R structures on the basis of the obtained orientation relations. Note that, for the R structure, the discussion here is restricted to the major $R1$ relation. To characterize the penetrated CN16 pairs, our first consideration is to the direction of a line connected between two center atoms of two CN16 polyhedra that form one penetrated CN16 pair. When this direction is referred to as the connected direction mentioned earlier, the relations obtained experimentally indicate that the connected direction in the α-Mn structure is parallel to the $[112]_\beta$ direction in the β-Mn structure. In the major $R1$ relation for the R structures, on the other hand, the connected direction corresponding to the $[0001]_R$ column-axis direction is nearly parallel to the $[\bar{4}13]_\beta$ direction. In addition to the connected direction, a bond length between two center atoms was also evaluated to be about 0.280 nm for the α-Mn structure and about 0.284 nm for the R structure by using the reported crystal-structure data on the α-Mn and R structures.[33,36] Based on these directions and lengths, we looked for structural units in the β-Mn structure. We found, as a result, that two types of penetrated CN14 pairs could be identified as structural units in the β-Mn structure. In one penetrated CN14 pair, its connected direction and bond length are, respectively, estimated to be the $[112]_\beta$ direction and about 0.268 nm.[34] In fact, this type of pairs was already shown in Figs. 1(a) and 1(a′). The other is also shown in Figs. 1(b) and 1(b′), and has the $[\bar{4}13]_\beta$ direction and a length of about 0.264 nm. This clearly indicates that the starting change for the (β-Mn$\rightarrow\alpha$-Mn) and (β-Mn$\rightarrow R$) structural changes can basically be characterized by the conversion from a penetrated CN14 pair to a penetrated CN16 one. It seems to us that the difference between the penetrated CN16 pairs in the α-Mn and R structures should originate from that between the penetrated CN14 pairs in the β-Mn structure.

The atomic shifts in the conversion between the penetrated CN14 and CN16 pairs for the (β-Mn$\rightarrow\alpha$-Mn) and (β-Mn$\rightarrow R$) structural changes are discussed on the basis of the above-mentioned relations between the penetrated pairs. As described in Sec. III, the conversion between the penetrated CN14 and CN16 pairs in the (β-Mn$\rightarrow\alpha$-Mn) change should occur by successive and simple atomic shifts. In this study, the atomic shifts in the conversion were actually determined by comparison between the reported atomic positions in the β-Mn and α-Mn structures[33,34] with the help of the obtained relation. The determined atomic shifts in the conversion between the penetrated pairs are depicted in Fig. 12. In the figure, the penetrated CN14 and CN16 pairs in the β-Mn and α-Mn structures are, respectively, indicated by the dashed and solid lines. Thus we conclude that the shifts indicated by the blue and red arrows are local and simple. In particular, two center atoms surrounded by the black squares move away very slightly in the conversion. In other words, there exists a one-to-one correspondence between the atomic positions of the penetrated CN14 pair in the β-Mn structure and the penetrated CN16 pair in the α-Mn structure.

Based on both the determined shifts in the conversion between the penetrated CN14 and CN16 pairs in Fig. 12 and the contrast change in Fig. 7, we discuss the formation process of the penetrated CN16 pair from the penetrated CN14 pair as the starting change in the (β-Mn$\rightarrow\alpha$-Mn) structural change. As discussed in Sec. III, the contrast change was found to consist of the first and second changes. In the calculated micrographs, specifically, the bright-contrast ring appears in the first change and the second change involves three steps: that is, the formation of (a) the bright-contrast line connected with two neighboring bright rings, (b) the dark-contrast ring, and (c) the dark-contrast line between two dark rings. Based on these contrast changes, it is clear that the conversion between the penetrated CN14 and CN16 pairs takes place by successive atomic shifts that occur with the lapse of time. We first consider the fact that the dark-contrast regions in the calculated micrographs correspond to the regions in which projected positions of atoms are densely arranged. Based on this, the bright-contrast ring in the first change should be formed by the atomic shifts indicated by the red arrows in Fig. 12. The other shifts indicated by the blue arrows must be associated with the second change involving the three steps. In other words, the first change ba-

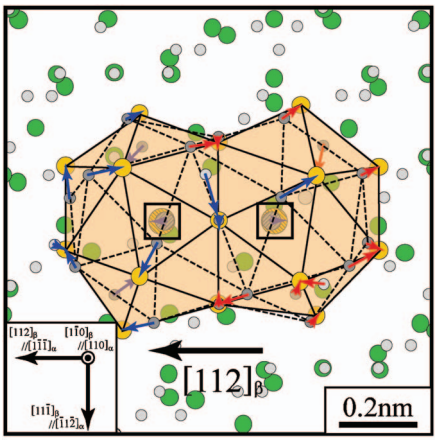

FIG. 12. (Color) Schematic showing determined atomic shifts in the conversion from a penetrated CN14 pair with the $[112]_\beta$ connected direction to a penetrated CN16 pair. The experimental data shown in Figs. 4 and 7 revealed that the (β-Mn$\rightarrow\alpha$-Mn) structural change started with this penetrated-pair conversion. Note that these penetrated CN14 and CN16 pairs were already shown in Figs. 1 and 2. In the diagram, the projected positions of atoms in the β-Mn structure are represented by the gray circles while the green and orange circles indicate those in the α-Mn structure. In particular, the orange circles show the projected positions in one penetrated CN16 pair produced by the conversion. The dashed and solid lines in the diagram also indicate the penetrated CN14 and CN16 pairs, respectively. The feature of the (β-Mn$\rightarrow\alpha$-Mn) change is that the penetrated-pair conversion occurs by successive atomic shifts. In the successive conversion, in fact, the atomic shifts indicated by the blue arrows follow those by the red arrows.

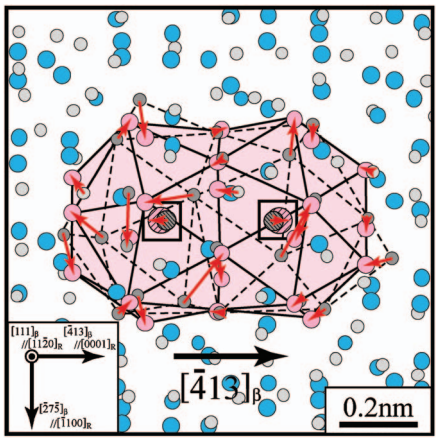

FIG. 13. (Color) Schematic showing determined atomic shifts in the conversion from a penetrated CN14 pair with the $[\bar{4}13]_\beta$ connected direction to a penetrated CN16 pair. The major $R1$ orientation relation derived from Fig. 8 indicated that the conversion between these penetrated pairs should occur in the initial stage of the (β-Mn$\rightarrow R$) structural change. Note that these penetrated CN14 and CN16 pairs were already shown in Figs. 1 and 2. In the diagram, the blue and pink circles represent the projected positions of atoms in the R structure, where the pink circles indicate the positions in one penetrated CN16 pair. Just as in the case of Fig. 12, the projected positions in the β-Mn structure are represented by the gray circles. The dashed and solid lines in the diagram also indicate the penetrated CN14 and CN16 pairs, respectively. From the diagram, the determined atomic shifts indicated by the red arrows are simple and small. There is a one-to-one correspondence between the atomic positions in these two penetrated pairs.

sically results in the formation of one CN16 polyhedron in the penetrated CN16 pair as an intermediate configuration. The penetrated CN16 pair in the α-Mn structure then appears via the formation of the other CN16 polyhedron in the second change. The intermediate configuration of the penetrated pair is a unique feature of the starting change in the (β-Mn$\rightarrow\alpha$-Mn) structural change.

As in the case of the (β-Mn$\rightarrow\alpha$-Mn) structural change, the essential feature of the (β-Mn$\rightarrow R$) change for the major $R1$ relation is also the conversion of a penetrated CN14 pair into a penetrated CN16 one. Because of the presence of the nanometer-sized atomic-column state, the direct conversion should first occur in the (β-Mn$\rightarrow R$) change, instead of the successive conversion in the (β-Mn$\rightarrow\alpha$-Mn) change. As a result of the direct conversion, the connected direction of a penetrated CN14 pair in the β-Mn structure becomes parallel to that of a penetrated CN16 pair, and corresponds to the $[0001]_R$ column-axis direction in the R structure. In other words, the directional relation for the major $R1$ relation is basically determined by the connected direction of a penetrated CN14 pair in the β-Mn structure. Figure 13 shows determined atomic shifts in the direct conversion between the penetrated CN14 and CN16 pairs for the $R1$ relation. In the determination of the shifts, we used the crystallographic data for the R structure that was reported by Shoemaker *et al.*[36] The dashed and solid lines in the diagram represent the penetrated CN14 pair with the $[\bar{4}13]_\beta$ connected direction in the β-Mn structure and the penetrated CN16 pair in the R structure, respectively. As is evident in the figure, the determined atomic shifts indicated by the red arrows are very local and simple. That is, there exists a one-to-one correspondence between atomic positions in the penetrated CN14 and CN16 pairs. The center atoms surrounded by the black square move away a little bit in the conversion, just as in the case of the (β-Mn$\rightarrow\alpha$-Mn) change. Although there is a difference between the formation processes of the penetrated CN16 pairs in the (β-Mn$\rightarrow\alpha$-Mn) and (β-Mn$\rightarrow R$) structural changes, the connected directions in the penetrated CN14 and CN16 pairs are understood to be maintained in both changes.

In this study, the minor $R2$ and $R3$ relations were also found in the (β-Mn$\rightarrow R$) structural change. The appearance of these minor relations may be caused by the addition of Si atoms because they were obtained mainly in alloys with higher Si contents. From the comparison between the atomic positions in the β-Mn and R structures for these minor relations, we conclude that the penetrated pair consisting of CN14 and CN12 polyhedra in the β-Mn structure is converted to the penetrated CN16 pair in the R structure for the $R2$ relation. For the $R3$ relation, on the other hand, neighboring CN14 and CN12 polyhedra in the β-Mn structure result in neighboring CN16 and CN12 polyhedra being involved in the atomic column of the R structure. The notable feature of the minor relations is that a CN12 polyhedron involved in the structural units of the β-Mn structure plays an important role in these two conversions. Figure 14 shows the deter-

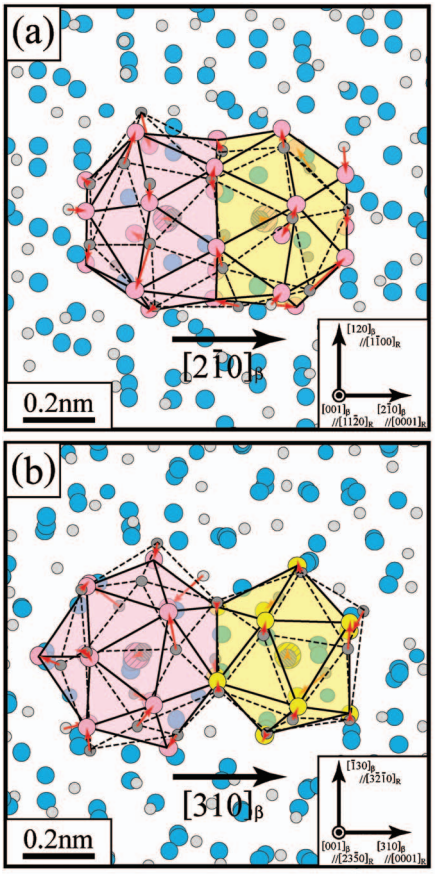

FIG. 14. (Color) Schematic showing determined atomic shifts in the structural-unit conversions for the minor $R2$ and $R3$ orientation relations in the (β-Mn$\rightarrow R$) structural change. In the structural change, two neighboring CN12 and CN14 polyhedra as a structural unit in the β-Mn structure are converted to one penetrated CN16 pair in the R structure for the $R2$ relation in (a), and to two neighboring CN12 and CN16 polyhedra for the $R3$ relation in (b). In other words, the conversion for the $R3$ relation just occurs between CN14 and CN16 polyhedra. In these diagrams, the dashed and solid lines indicate the above-mentioned structural units in the β-Mn and R structures, respectively.

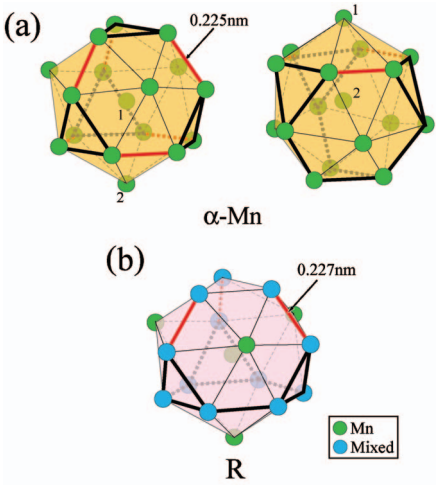

FIG. 15. (Color) Schematic of CN16 polyhedra forming the penetrated CN16 pairs involved in the α-Mn and R structures. There is a difference between two CN16 polyhedra in one penetrated CN16 pair for the α-Mn structure while one CN16 polyhedron for the R structure is identical to the other. In the figure, these two CN16 polyhedra in the α-Mn structure and one CN16 polyhedron in the R structure are then shown in (a) and (b), respectively. For the α-Mn structure in (a), the atoms numbered by 1 and 2 in the left CN16 polyhedra are the same as those in the right CN16 polyhedron.

mined atomic shifts in the structural-unit conversions for the $R2$ and $R3$ relations. For both the $R2$ relation in (a) and the $R3$ relation in (b), the shifts indicated by the red arrows are understood to be local and simple. This confirms that, for the $R2$ and $R3$ relations, there is one-to-one correspondence between the atomic positions in the structural units for the β-Mn and R structures, just as in the case of the $R1$ relation. The directional relations in the orientation relationship for the minor relations are also determined by the directions connected between two center atoms of the structural units in the β-Mn structure. That is, the directions are parallel to the $[2\bar{1}0]_\beta$ direction for the $R2$ relation and the $[310]_\beta$ direction for the $R3$ relation.

There is no doubt that the stability of the CN12 polyhedron in the β-Mn structure is crucial for the appearance of the $R2$ and $R3$ relations. It is likely that the addition of Si atoms with a smaller atomic size would influence the stability of the CN12 polyhedron. The point to note here is that the addition of Si atoms into the β-Mn structure with only Mn atoms may lead to charge transfer between Mn and Si atoms. Both the charge transfer and a smaller atomic size would prefer to compact structural units such as a CN12 polyhedron: that is, an icosahedral atomic cluster. Because the R structure appearing because of the Si-atom addition is characterized by the array of atomic columns involving the CN12 polyhedra, the stability of the R structure may be related to that of the CN12 polyhedron.

The complicated antiferromagnetic ordering was reported in the α-Mn structure that is characterized by a periodic array of penetrated CN16 pairs.[33,44–49] In the R structure, on the other hand, it was suggested that a penetrated CN16 pair in an atomic column is involved in atomic bonding with covalentlike character.[42] Based on this, we are very interested in the interplay between the appearance of a local magnetic moment and the formation of covalentlike bonding. Because this interplay would be sensitive to both site occupancies of atoms and atomic-bond lengths, we evaluated these values in the penetrated CN 16 pairs for the α-Mn and R structures using the reported crystal-structure data.[33,36] It should here be noted that, in the penetrated CN16 pair of the α-Mn structure, one CN16 polyhedron is different from the other. The presence of these two kinds of CN16 polyhedra should be associated with the successive conversion in the (β-Mn$\rightarrow\alpha$-Mn) structural change. Then, both the CN16 polyhedra in the α-Mn structure and the CN16 polyhedron in the R structure are schematically depicted in Fig. 15. In the figure, the thick black lines indicate atomic bonds with lengths of less than 0.245 nm except for the shortest bonds in the α-Mn and R structures. The shortest atomic bonds are marked by the thick red lines, and their lengths are estimated

to be about 0.225 nm for the α-Mn structure and about 0.227 nm for the R structure. Although each atomic-bond length is not specified in the diagrams, there is no essential difference between the CN16 polyhedron in the R structure and the two kinds of CN16 polyhedra in the α-Mn structure, with respect to the atomic-bond length. We then look at an inner CN12 polyhedron in each CN16 polyhedron which consists of atoms connected by the shorter atomic bonds with lengths of less than 0.245 nm. The inner CN12 polyhedron is obviously not an icosahedral atomic cluster but is usually called a Friauf polyhedron. When we focus on Friauf polyhedra, the difference between the α-Mn and R structures is found to be just the site occupancies of atoms. Only Mn atoms indicated by the green circles occupy the atomic sites in the α-Mn structure of the metallic Mn. Based on the crystallographic data reported by Shoemaker *et al.*,[36] on the other hand, all atomic sites of the Friauf polyhedron in the R structure are understood to be mixed sites consisting of Mn and Si atoms. Note that the blue circles in (b) represent atoms in the mixed sites. The mixed sites are obviously produced by the addition of Si atoms, and may lead to charge transfer between Mn and Si atoms. Based on this, it seems to us that charge transfer is one of the crucial factors in the formation of covalentlike bonding in the Friauf polyhedron[50,51] of the R structure. It can even be suggested that the charge transfer produced by the addition of Si atoms should play a crucial role in both the suppression of the complicated antiferromagnetic ordering and the formation of the Friauf polyhedron with covalentlike bonding.

V. CONCLUSIONS

The crystallographic features of the (β-Mn$\rightarrow\alpha$-Mn) and (β-Mn$\rightarrow R$) structural changes related to the (β-Mn$\rightarrow\alpha$-Mn+R) eutectoid reaction in the Mn-Si alloy system have been examined so as to understand the characteristic features of a structural change between two coordination-polyhedra structures. Only one orientation relation was found in the former (β-Mn$\rightarrow\alpha$-Mn) change. In this change, successive atomic shifts resulted in the formation of penetrated CN16 pairs from the penetrated CN14 pair. On the other hand, there exist three types of orientation relations in the latter (β-Mn$\rightarrow R$) change. Among the three relations, the penetrated CN16 pair in the R structure is directly converted from the penetrated CN14 pair in the β-Mn structure for the major relation. As for two other minor relations found in alloys with higher Si contents, CN12 polyhedra stabilized by the addition of Si atoms may play a certain role in the structural-unit conversions. As a result of these conversions, the directional relation in the orientation relationship for the (β-Mn$\rightarrow\alpha$-Mn) and (β-Mn$\rightarrow R$) structural changes is determined by the connected direction between two center atoms in the penetrated CN14 pairs or the structural units consisting of two neighboring polyhedra in the β-Mn structure. In other words, the crucial factor controlling the structural changes should be the conversion between the structural units that consist of only two neighboring polyhedra involved in these complex structures, including the penetrated CN14 and CN16 pairs. To understand the interplay between the appearance of a magnetic moment in the α-Mn structure and the formation of covalentlike bonding in the R structure we evaluated both site occupancies of atoms and atomic-bond lengths of CN16 polyhedra in the penetrated CN16 pair for the α-Mn and R structures. This evaluation suggests that, because the addition of Si atoms would results in charge transfer between Mn and Si atoms, the formation of a Friauf polyhedron with covalentlike bonding in the R structure might be responsible for the suppression of the complicated antiferromagnetic ordering in the α-Mn structure. Note that a Friauf polyhedron[50,51] with CN12 is distinct from an icosahedral atomic cluster and is present as an inner CN12 polyhedron in a CN16 polyhedron. We believe that the results obtained in this study help a deeper understanding of the metallic-glass and amorphous states as well as the crystal structures of both the quasicrystals and related approximant phases.

[1] D. Shechtman, I. Blech, D. Gratias, and J. W. Cahn, Phys. Rev. Lett. **53**, 1951 (1984).
[2] D. Levine and P. J. Steinhardt, Phys. Rev. Lett. **53**, 2477 (1984).
[3] D. Levine and P. J. Steinhardt, Phys. Rev. B **34**, 596 (1986).
[4] J. E. S. Socolar and P. J. Steinhardt, Phys. Rev. B **34**, 617 (1986).
[5] L. Bendersky, Phys. Rev. Lett. **55**, 1461 (1985).
[6] A. L. Mackay, Acta Crystallogr. **15**, 916 (1962).
[7] M. Audier and P. Guyot, Philos. Mag. B **53**, L43 (1986).
[8] V. Elser and C. L. Henley, Phys. Rev. Lett. **55**, 2883 (1985).
[9] G. Bergman, J. L. T. Waugh, and L. Pauling, Acta Crystallogr. **10**, 254 (1957).
[10] V. Elser, Acta Crystallogr., Sect. A: Found. Crystallogr. **42**, 36 (1986).
[11] A. P. Tsai, J. Q. Guo, E. Abe, H. Takakura, and T. J. Sato, Nature (London) **408**, 537 (2000).
[12] M. Boström and S. Hovmöller, Acta Crystallogr., Sect. B: Struct. Sci. **57**, 646 (2001).
[13] G. Kreiner and H. F. Franzen, J. Alloys Compd. **221**, 15 (1995).
[14] D. Romeu, Philos. Mag. B **67**, 77 (1993).
[15] T. Ishimasa, H.-U. Nissen, and Y. Fukano, Phys. Rev. Lett. **55**, 511 (1985).
[16] H. Chen, D. X. Li, and K. H. Kuo, Phys. Rev. Lett. **60**, 1645 (1988).
[17] T. Takagi, T. Ohkubo, Y. Hirotsu, B. S. Murty, K. Hono, and D. Shindo, Appl. Phys. Lett. **79**, 485 (2001).
[18] J. Saida and A. Inoue, J. Non-Cryst. Solids **317**, 97 (2003).
[19] T. Fukunaga, K. Itoh, T. Otomo, K. Mori, M. Sugiyama, H. Kato, M. Hasegawa, A. Hirata, Y. Hirotsu, and A. C. Hannon, Mater. Trans. **48**, 1698 (2007).
[20] X. Hui, H. Z. Fang, G. L. Chen, S. L. Shang, Y. Wang, and Z. K. Liu, Appl. Phys. Lett. **92**, 201913 (2008).
[21] A. Hirata, Y. Hirotsu, K. Amiya, and A. Inoue, Phys. Rev. B **78**, 144205 (2008).

[22] A. Hirata, Y. Hirotsu, K. Amiya, and A. Inoue, Phys. Rev. B **79**, 020205(R) (2009).
[23] M. Imafuku, S. Sato, H. Koshiba, E. Matsubara, and A. Inoue, Scr. Mater. **44**, 2369 (2001).
[24] M. Shapaan, J. Lábár, J. Lendvai, and L. K. Varga, Mater. Sci. Eng., A **375-377**, 789 (2004).
[25] D. H. Kim, J. M. Park, D. H. Kim, and W. T. Kim, J. Mater. Res. **22**, 471 (2007).
[26] A. Inoue, B. L. Shen, and C. T. Chang, Intermetallics **14**, 936 (2006).
[27] A. Hirata, Y. Hirotsu, E. Matsubara, T. Ohkubo, and K. Hono, Phys. Rev. B **74**, 184204 (2006).
[28] J. Donohue, *The Structures of the Elements* (Wiley, New York, 1974).
[29] A. J. Bradley and J. Thewlis, Proc. R. Soc. London, Ser. A **115**, 456 (1927).
[30] G. D. Preston, Philos. Mag. Series 7 **5**, 1207 (1928).
[31] S. Samson, in *Structural Chemistry and Molecular Biology*, edited by A. Rich and N. Davidson (Freeman, San Francisco, London, 1969).
[32] W. B. Pearson, *The Crystal Chemistry and Physics of Metals and Alloys* (Wiley, New York, 1972).
[33] T. Yamada, N. Kunitomi, Y. Nakai, D. E. Cox, and G. Shirane, J. Phys. Soc. Jpn. **28**, 615 (1970).
[34] C. B. Shoemaker, D. P. Shoemaker, T. E. Hopkins, and S. Yindepit, Acta Crystallogr., Sect. B: Struct. Crystallogr. Cryst. Chem. **34**, 3573 (1978).
[35] D. I. Bardos and P. A. Beck, Trans. Metall. Soc. AIME **233**, 1446 (1965).
[36] C. B. Shoemaker and D. P. Shoemaker, Acta Crystallogr., Sect. B: Struct. Crystallogr. Cryst. Chem. **34**, 701 (1978).
[37] P. F. Wieser and W. D. Forgeng, Trans. Metall. Soc. AIME **230**, 1675 (1964).
[38] A. Hirata, Y. Koyama, and M. Tanimura, Phys. Rev. B **67**, 144107 (2003).
[39] A. Hirata and Y. Koyama, Phys. Rev. B **70**, 134203 (2004).
[40] A. Hirata, A. Iwai, and Y. Koyama, Phys. Rev. B **74**, 054204 (2006).
[41] T. Doi, M. Tanimura, and Y. Koyama, Phys. Rev. B **79**, 134204 (2009).
[42] T. Doi, M. Tanimura, and Y. Koyama, Phys. Rev. B **77**, 134205 (2008).
[43] C. P. Heijwegen and G. D. Rieck, J. Less-Common Met. **37**, 115 (1974).
[44] C. G. Shull and M. K. Wilkinson, Rev. Mod. Phys. **25**, 100 (1953).
[45] J. A. Oberteuffer, J. A. Marcus, L. H. Schwartz, and G. P. Felcher, Phys. Lett. A **28**, 267 (1969).
[46] N. Kunitomi, Y. Yamada, Y. Nakai, and Y. Fujii, J. Appl. Phys. **40**, 1265 (1969).
[47] A. C. Lawson, A. C. Larson, M. C. Aronson, S. Johnson, Z. Fisk, P. C. Canfield, J. D. Thompson, and R. B. Von Dreele, J. Appl. Phys. **76**, 7049 (1994).
[48] H. Yamagata and K. Asayama, J. Phys. Soc. Jpn. **33**, 400 (1972).
[49] D. Hobbs, J. Hafner, and D. Spišák, Phys. Rev. B **68**, 014407 (2003).
[50] J. B. Friauf, Phys. Rev. **29**, 34 (1927).
[51] S. Samson, Acta Crystallogr. **11**, 851 (1958).